



Secondary electron yield reduction of copper after 355 nm ultrashort pulse laser ablation

Pierre Lorenz¹ · Marcel Himmerlich² · Martin Ehrhardt¹ · Elena Bez^{2,3} · Karolina Bogdanowicz² · Mauro Taborelli² · Klaus Zimmer¹

Accepted: 7 February 2022 / Published online: 3 March 2022
© The Author(s) 2022

Abstract

Nanostructured surfaces exhibit remarkable chemical, physical and microbiological properties and have therefore various technical and industrial applications. The ultrashort laser pulse irradiation (wavelength $\lambda = 355$ nm, pulse duration $\Delta t_p = 12$ ps, repetition rate $f = 100$ kHz) of copper samples with appropriate laser parameters results in the formation of a micro- and nanostructured surfaces. The influence of these hierarchically textured surfaces on the secondary electron yield (SEY) was studied especially with regard to their morphological and geometrical properties. Specific SEY changes are caused by both, the shape and the depth of the microstructures, as well as the morphology of the formed nanostructures; that can be either compact flower head-like nanostructures, non-compact filament-shaped nanostructures, molten and resolidified spherical structures, or minor modified surfaces. The measured SEY as a function of the primary electron energy is correlated with the surface topography that forms upon laser irradiation. The SEY decreases with increasing accumulated laser fluence and ablated volume, respectively. Especially flower-head-like nanostructures can be produced at high laser power ($P \geq 400$ mW) and low scanning velocity ($v \leq 10$ mm/s) and represent a surface with strongly reduced SEY maximum as low as 0.7.

Keywords ps-laser · Ablation · Surface modification · Secondary electron yield · Copper · Black copper · Surface topography · Nanostructure · SEY

✉ Pierre Lorenz
pierre.lorenz@iom-leipzig.de

¹ Department of Ultra-Precision Surfaces, Leibniz Institute of Surface Engineering (IOM), Permoserstr. 15, 04318 Leipzig, Germany

² CERN, European Organization for Nuclear Research, CH-1211, Geneve 23, 1211 Geneva, Switzerland

³ University of Leipzig, Linnéstr. 5, 04103 Leipzig, Germany

Introduction

The short and ultrashort laser pulse irradiation of copper surfaces allows generating geometrical, chemical, structural, and morphological surface modifications. Laser ablation processes inducing copper surface modification were reported for pulsed irradiation with different pulse duration and laser wavelength [1, 3, 5, 15, 18, 20–22, 26, 28, 29, 31, 33, 41, 42, 44]. Laser ablation was studied for ns- [3, 14, 18, 23, 33, 37], ps- [5, 13, 15, 20, 22, 23, 29, 41, 42, 44] and fs-laser irradiation [15, 20, 26, 28, 29, 41, 42, 44] with wavelengths from ultraviolet to infrared. The ablation was furthermore investigated as a function of several other laser parameters such as the wavelength λ [33], the pulse duration Δt_p [15, 29, 41], the number of laser pulses N [5], the laser pulse energy E [33], the repetition rate f [20, 28], as well as multi-pulse irradiation (burst) [4, 44]. Usually, a complex correlation of the laser processing parameters and the resulting ablation characteristics, such as the ablation volume V_{ab} , the shape of the formed crater, the crater width d and depth Δz , are observed. In general, the ablated volume increases with higher laser pulse energy [29]. Typically the ablation process is more effective in case of UV irradiation compared to IR laser sources [33]. Fan et al. [11] reported experiments on the irradiation of copper with an IR ps-laser, and found at suitable laser parameters the formation of a nanostructured surface induced by a redeposition process. The size and number of the formed nanoparticles are dependent on the laser processing parameters, especially the scanning speed [11]. The related ablation processes were also studied for different gas environments [3, 31] and for additional external magnetic fields [23]. Also, the pulsed laser deposition (PLD) of copper surfaces at ambient pressure results in the formation of a chain-shaped nanostructure at the copper surface [12]. Besides the characterization of the ablation structures by surface sensitive techniques, the dynamics of the ablation process was also studied by shadowgraphy [23]. The ablation process was described in a thermodynamic model. At ultrashort laser pulses, a two-temperature model can be used to describe the laser-solid interaction [1, 6]. A hybrid simulation, that couples the finite difference method to solve the heat transfer equations with molecular dynamics calculations, allows a good description of the ablation mechanism [27]. The ablation process of metal surfaces results, in addition to ablation pits, for suitable laser parameters in the formation of a nanostructured surface [31] with interesting and adjustable physical quantities, such as low reflectivity [31] and low secondary electron yield (SEY) [2, 7, 8, 14, 32, 34–37, 39, 40] enabling multiple applications [2, 11, 12, 39]. SEY is the physical quantity which governs multipacting in radiofrequency devices, charging phenomena in satellites and electron cloud in particle accelerators. In particular, in cryogenic section of accelerators, as for the Large Hadron Collider (LHC), it is responsible of a large fraction of the beam-induced heat-load to be dissipated by the cryogenic plant. Effects of laser-treatment on SEY was mainly studied at $\lambda = 532$ nm [7, 8, 35]. In this study, the UV ps-laser treatment of copper surfaces was investigated with the aim to produce nanostructured surfaces with reduced secondary electron yield (SEY) to extend the knowledge of laser-induced nanostructure formation process

and the laser-induced SEY reduction. The focus of the performed experiments is the analysis of correlations between surface morphology and the SEY.

Experimental Details

Polycrystalline copper samples (oxygen-free electronic grade – OFE, size: $20 \times 20 \times 1 \text{ mm}^3$) were degreased by a commercial detergent and subsequently passivated in a chromic acid solution. These samples were mounted onto an x-y-stage of a laser workstation from 3D-Micromac. The sample surface was irradiated in air by a Nd:YVO₄ laser with a pulse duration of $\Delta t_p = 12 \text{ ps}$, a repetition rate of $f_{\text{rep}} = 100 \text{ kHz}$, and a wavelength of $\lambda = 355 \text{ nm}$. A galvo scanner is advancing the laser spot across the sample surface at a velocity v . This scanning velocity was varied from 1 to 200 mm/s. The laser beam was focused onto the sample surface by a f-theta lens having a focal length of 103 mm. The Gaussian laser beam spot radius ω ($14.6 \pm 1.5 \text{ } \mu\text{m}$) was determined by Liu's method [19]. The irradiation scheme is based on the creation of parallel lines with a spacing Δy (see Fig. 1). First, single non-overlapping lines ($\Delta y \gg 2\omega$) were produced to characterize the ablation behaviour. In a second step, large areas were laser-textured with a partial overlap of the scan lines with $\Delta y = 10 \text{ } \mu\text{m}$. The number of accumulated laser pulses on the same surface point for non-overlapping line experiments can be estimated by:

$$N_l = \frac{f_{\text{rep}} \cdot 2\omega}{v} \quad (1)$$

and for overlapping lines: by

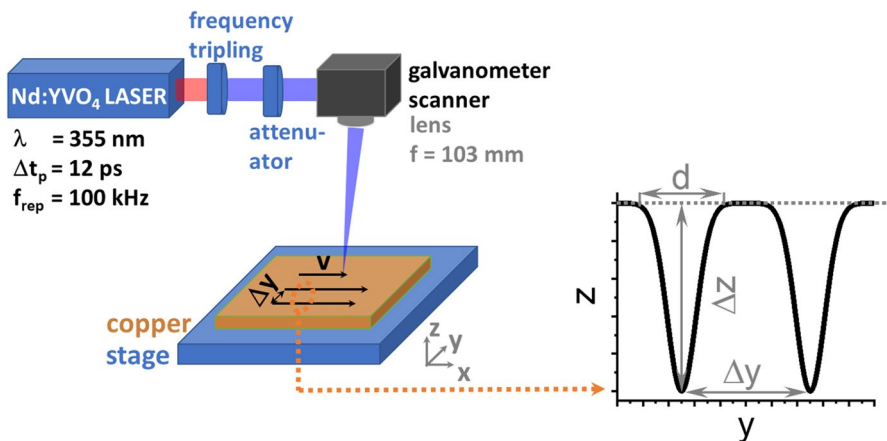


Fig. 1 Schematic illustration of the experimental setup for UV ps-laser treatment

$$N_a = \frac{frep \cdot \pi \omega^2}{v \cdot \Delta y} \quad (2)$$

The surface morphology of the laser-treated copper surfaces was analysed using optical microscopy (OM), scanning electron microscopy (SEM) and white light interferometry (WLI). For trench profile analysis of the non-overlapping lines, the irradiated line patterns were mechanically wipe-cleaned using propanol-immersed cotton and subsequently underwent ultrasonication in propanol to remove any re-deposited material and particles inside the trenches. For cross section preparation, large-area machined samples were embedded in a transparent resin, ground with SiC papers down to grit P1200 and subsequently polished in sequence with 3 μm and 1 μm diamond suspensions, respectively. These cross sections were characterized using a digital microscope (KEYENCE VHX 6000). The secondary electron yield (SEY) was measured for primary electron energies between 50 and 1800 eV on 20 \times 20 mm² homogeneously laser-treated samples. The details of the utilized setup and the implemented experimental conditions for SEY analyses are described in Ref. [24].

Results and Discussion

Characterization of the laser ablation

The single line laser scribing across the copper surface (see Fig. 1) leads to the formation of trenches with a truncated “Gaussian-shaped” cross section. If the line distance Δy is much larger than the Gaussian radius ω , interaction phenomena within the laser process due to redeposited material from previous trench ablation of the nearby line do not occur. The laser-induced trenches were analysed by white light interferometry (WLI). First, the trench depth Δz and trench width d (defined in Fig. 1) were determined in dependence of the laser power P and the scanning speed v .

Both, trench depth and width are increasing for increasing laser power P and decreasing for increasing velocity v , as visualized in Fig. 2(a–d). The increase of the trench depth Δz with increasing laser power P confirms earlier experimental studies [6, 33]. Moreover, the trench depth Δz increases with decreasing scanning velocity, in agreement with other reports on laser ablation of copper [9]. The increase of the trench width at decreasing scanning speed and increasing number of laser pulses N is induced by incubation effects [16], i.e. a reduction of the ablation threshold P_{th} for increasing number of laser pulses N on the same surface location. For extremely low scanning speeds, thermal accumulation [25] may also be relevant.

The laser power distribution for a Gaussian laser beam profile is given by:

$$P(r) = P_0 \cdot e^{-2r^2/\omega^2} \quad (3)$$

with the Gaussian radius ω , the spatial distance r to the centre of the laser spot, and the maximum laser power P_0 in the laser spot centre. The accumulated number

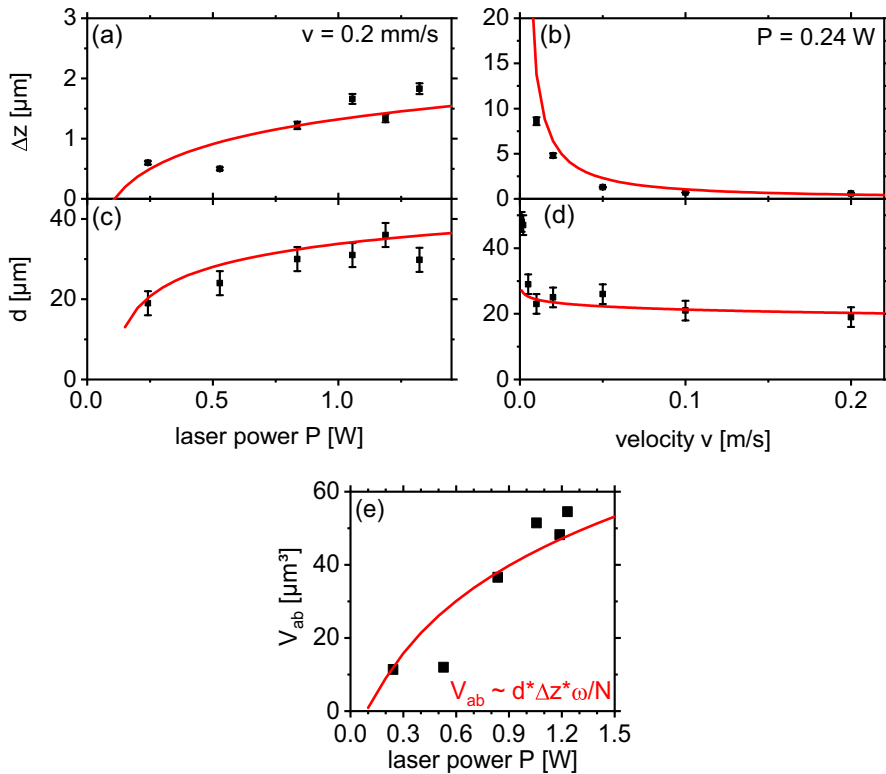


Fig. 2 Depth Δz ((a), (b)) and width d ((c), (d)) of single trenches, as determined by WLI measurements, in dependence of the laser power P and the scanning velocity v (black dots). The red lines are fits to the data using the model described by Eqs. 5 and 7. (e) Laser power dependence of the ablation volume V_{ab} per laser pulse as determined from WLI profiling within cleaned trenches at a scanning speed $v = 200$ mm/s (red line: estimated ablation volume V_{ab})

of laser pulses N is dependent on the scanning velocity v , the repetition rate f_{rep} , and the Gaussian radius ω (Eqs. 1 and 2). This incubation effect can be empirically described by [10]:

$$P_{th}(N) = P_{th}(1) \cdot N^{S-1} \rightarrow P_{th}(v) = P_{th}(1) \cdot \left(\frac{f_{rep} \cdot 2\omega}{v} \right)^{S-1} \quad (4)$$

With S being the incubation coefficient. After substitution of Eq. 4 into Eq. 3, the trench width d can be calculated by:

$$d(v, P) = \omega \sqrt{2 \cdot \ln \left(\frac{P}{P_{th}(1) \cdot \left(\frac{f_{rep} \cdot 2\omega}{v} \right)^{S-1}} \right)} \quad (5)$$

Based on Eq. 5, the experimentally determined dependencies of the trench width on the velocity v and the laser power P were fitted (red lines in Fig. 2(c),(d)). The obtained fit parameters are summarized in Table 1. Assuming that the ablation depth Δz is given by the effective penetration depth (α_{eff}^{-1}) of the laser light according to the Beer-Lambert law, and considering that the ablation threshold (P_{th}) must be exceeded, the ablation depth can be estimated by:

$$P(z) = P_0 \cdot e^{-\alpha_{eff} \cdot z} \rightarrow \Delta z(P) = \frac{1}{\alpha_{eff}} \ln \left(\frac{P}{P_{th}} \right) \quad (6)$$

The substitution of Eq. 4 into Eq. 6 allows the description of the trench depth Δz in dependence of the processing parameters (scanning speed v and laser power P):

$$\Delta z(v, P) = \frac{1}{\alpha_{eff}} \ln \left(\frac{P}{P_{th}(1) \cdot \left(\frac{f_{rep} \cdot 2\omega}{v} \right)^{S-1}} \right) \cdot (f_{rep} \cdot 2\omega) / v \quad (7)$$

Based on Eq. 7, the dependencies of the trench depth on the velocity v and the laser power P were fitted (red lines in Fig. 2 (a), (b), fit parameters listed in Table 1). In agreement with the increase of the trench depth and width at increasing laser power, the ablation volume increases as well. Figure 2(e) presents the determined ablation volume V_{ab} in dependence of the laser power P at $v = 200$ mm/s. In addition, the ablation volume per laser pulse can be described by $V_{ab} = d \cdot \Delta z \cdot \omega / N$ with d , Δz , and N being calculated from Eqs. 5 to 7, and Eq. 1, respectively, and using the obtained parameters from the fit procedure that are summarized in Table 1. Furthermore, the dependence of the ablation volume on the laser power allows the estimation of the ablation threshold, which is ~ 0.088 mW at $v = 200$ mm/s (corresponds to $N = 14.6$). The value agrees with the ablation threshold calculated by Eq. 4 of $P_{th}(v = 200 \text{ mm/s}) = 0.082$.

This semi-empirical approach based on Eqs. 5 and 7 allows a good description of the experimental results. The determined absorption coefficient α_{eff} (Table 1) is of the same order of magnitude as the linear absorption coefficient of copper, which is $6.8 \cdot 10^7 \text{ m}^{-1}$ [17]. The estimated ablation threshold of 0.13 W corresponds to a laser fluence threshold of $\sim 0.4 \text{ J/cm}^2$. The value is of the same order of magnitude as the published value for 532 nm, which is $\sim 0.24 \text{ J/cm}^2$ [2].

The incubation factor S of 0.83 is almost similar to the reported value of $S = 0.7$ using a IR ps-laser [43].

Table 1 Summary of the parameters determined by iterative fitting Eqs. 5 and 7 to the experimental results in Fig. 2

$P_{th}(1)$ [W]	0.13
S	0.83
α_{eff} [m^{-1}]	$2.8 \cdot 10^7$

Two-dimensional laser irradiation

The laser irradiation of the copper surface utilizing overlapping lines of small distance (Δy is about the size of the Gaussian radius) allows a large area modification of the surface. In Fig. 3(a), a photograph of laser-treated sample is shown. For each sample, 64 regions were modified using different laser treatment parameters. The laser power was varied from 1.23 to 0.01 W (from top to bottom) and the scanning velocity from 1 to 200 mm/s (from left to right).

The photograph (Fig. 3(a)) reveals the modification of the optical appearance for different treatment parameters that spans from weak colouring, changed reflectivity to completely dark surfaces. In particular, dark surfaces (low reflectivity) can be created at high laser power P and low scanning velocity v . Figure 3(b–e) includes SEM images and optical cross section images of the region marked in Fig. 3(b), that was irradiated with a scanning speed of $v = 1$ mm/s, a laser power of $P = 1.23$ W and a line distance of $\Delta y = 10$ μm . The nanostructured morphology of the surface is visible in the SEM image at higher magnification, which is due to redeposition of nanoparticles on top of the micrometer-sized textured copper sample, as seen in the cross sections. The surface appears homogeneous, and the top-view SEM measurements do not clearly show the underlying trench-topography. In Figs. 4 and 5, the surface topography as well as the cross section of selected samples dependent on the laser parameter (laser power P and scanning speed v) are summarized for the complete explored parameter range.

Based on the shape of the nanostructures at the copper surface, the laser parameter field can be subdivided into four groups showing a particular type of morphology (see Fig. 4 surrounded by colour lines):

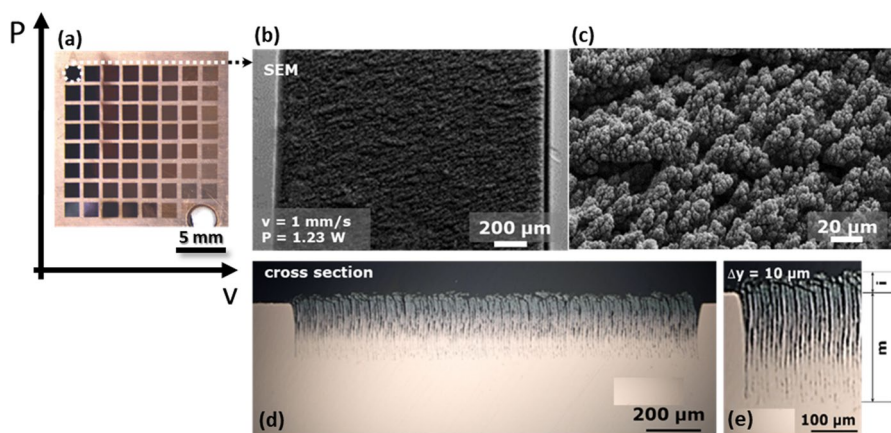


Fig. 3 (a) Photographs of laser-treated Cu samples irradiated with different scanning velocities v [mm/s] = 1, 2, 5, 10, 20, 50, 100, 200 (from left to right) and laser power at 355 nm P [W] = 1.23, 1.19, 1.06, 0.84, 0.53, 0.24, 0.06, 0.01 (from top to bottom). (b), (c) Selected scanning electron micrographs at different magnification of a surface created at $P = 1.23$ W and $v = 1$ mm/s, $\Delta y = 10$ μm . (d), (e) Optical Micrographs of the near-surface cross section of the same sample

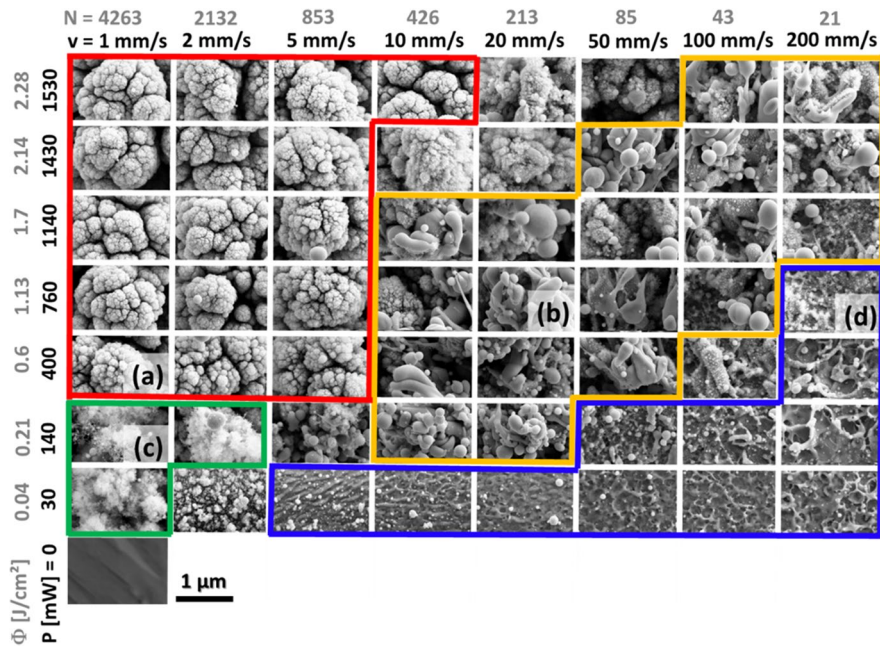


Fig. 4 SEM images of laser-treated copper surfaces ($\lambda=355$ nm, $f=100$ kHz, $\Delta y=10$ μm) at different laser power P (grey: calculated laser fluence Φ) and scanning speed v (grey: calculated number of laser pulses N based on Eq. 2). Based on the different shapes of the formed surface structures, the complete parameter field can be separated in four different zones with different surface morphology. Exemplary SEM images of the four processing parameter ranges are marked with (a–d) and are shown magnified in Fig. 5

- **Compact & dense, flower-head-like nanostructures** ($P \geq 400$ mW, $v \leq 10$ mm/s, marked red)
- **Non-compact filament-shaped nanostructures** ($P \leq 140$ mW, $v \leq 2$ mm/s, marked green)
- **Molten and resolidified spherical structures** ($v \geq 10$ mm/s, size < 1 μm , marked yellow)
- **Minor modified surface** ($P \leq 760$ mW, $v \geq 5$ mm/s, size < 150 nm, marked blue)

Selected cross sections were prepared in the different modification zones. Optical images of the cross sections for the four different laser parameter groups are shown in Fig. 5. The cross sections below the SEM images reveal the microscopic substructure of the samples as created by the laser–material interaction.

Within the red-marked laser parameter range, the irradiation results in the formation of compact and dense, flower head-like surface nanostructures as seen in Fig. 5(a). A similar structure is shown in Fig. 3(d) and (e) for the sample processed using a laser power of 1230 mW and a scanning speed of 1 mm/s, where the respective cross section is shown for two different magnifications. These

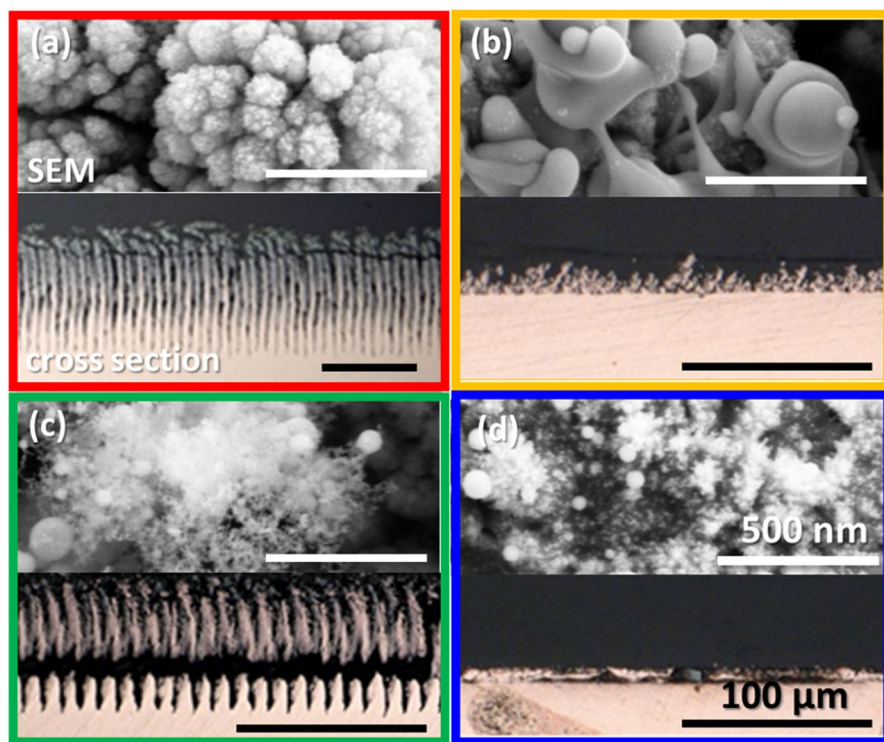


Fig. 5 SEM top view and optical cross-sectional images of the four classified surface modification types. The colour of the frames is related to the modification type (see Fig. 5). (a) $P=400$ mW, $v=1$ mm/s (red), (b) 760 mW, 20 mm/s (yellow), (c) 140 mW, 1 mm/s (green), (d) 760 mW, 200 mm/s (blue). The white scale bar corresponds to length of 500 nm which is constant for all 4 SEM images, while the black scale bars correspond to a length of 100 μm (the optical micrographs were measured at different magnification)

cross-section images indicate a modification depth m of approximately 211 μm that is covered by an additional redeposited nanostructured layer of ~ 28 μm thickness. The reduction of the laser power to 400 mW ($v=1$ mm/s, see Figs. 4 and 5(a), red-marked parameter range) results in a reduction of the texture depth to ~ 108 μm . In this case, the redeposited layer had a thickness of ~ 31 μm .

For the red-marked laser parameter range, the laser power is significantly higher than the ablation threshold and a distinctly higher ablation volume is expected, i.e. a higher number of particles are available for the redeposition process. The resulting texture depth and the ablated volume both increase for a higher laser power or when reducing the scanning speed.

Beside the ablation volume, the amount of the redeposited material on laser processed surface is additionally influenced by secondary effects. The laser ablation process results in the formation of an expanding laser plume with a high local pressure inside, which results in an expansion of the plume, and consequently defines the formation, scattering as well as deposition of the particles [30].

Furthermore, the small scanning velocity causes an additional laser irradiation of the redeposited material and results in a modification of it. This additional laser tempering process results most likely in the formation of the existing compact nanostructures at the surface. Similar compact flower head-like copper nanostructures were also reported by Calatroni et al. [6] using a ps-laser with a wavelength of $\lambda = 532$ nm and a pulse duration of $\Delta t_p = 10$ ps. In addition, also the utilisation of UV and IR ns laser radiation results in the formation of compact nanostructures [14, 36, 37].

It seems that the resulting nanostructures appear independent of the used laser wavelength and pulse duration. This confirms the conclusion that the nanostructure formation on top of the ablated grooves is explained by a redeposition process. However, the proportion and the morphology of the redeposited material depends on the characteristics of the ablation process, which is defined by the laser processing parameters.

The reduction of the laser power (green-marked parameter range) results in the formation of non-compact filament-shaped nanostructures. At a laser power of 140 mW and $v = 1$ mm/s (see Fig. 6(c)) the texture depth m reduces to ~ 20 μm . The distance of the periodic textures corresponds to the scanning scheme and the line distance of 10 μm . For the green-marked parameter range, the laser power is close to the ablation thresholds. An ablation threshold of ~ 30 mW at 1 mm/s can be estimated (based on Table 1 and Eq. 4). The redeposition process results here in the formation of non-compact nanostructures. Similar structures were found at pulsed laser deposition (PLD) of copper using picosecond laser irradiation in air. The PLD induced copper particles presented a high tendency to agglomerate and form chain-like structures [13].

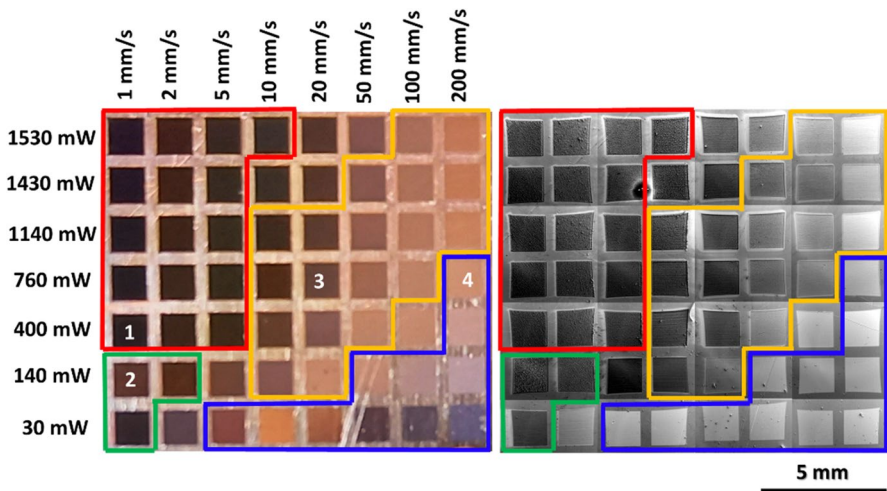


Fig. 6 (Left) Optical micrograph of the laser-treated copper surface (positions 1–4 mark the parameters for which the surface topography and cross sections are shown in Fig. 6). (Right) SEM images of the same laser treated copper sample with $\lambda = 355$ nm, $f = 100$ kHz, $\Delta y = 10$ μm at 5 keV primary electron energy

The utilisation of higher scanning speed (yellow laser parameter range) results in the formation of molten and resolidified spherical structures (see Figs. 4 and 5(b)). At a scanning speed of $v=20$ mm/s and a laser power of $P=760$ mW (see Fig. 5(b)), the resolidified structures exhibit an average texture depth of $m\sim 16$ μm . For low scanning speed v and low laser power P (blue laser parameter range) only minor surface modifications occur, consistent with a low texture depth. For example, at a laser power of $P=760$ mW and a scanning speed of $v=200$ mm/s, a texture depth of $m=8$ μm was found. For the yellow and blue laser parameter ranges, the ablation volume is small and melting processes mainly dominate the surface modification process. The surface tension and the laser-induced temperature gradient result in a mass flow of the liquid before cool-down and results in solidified micro- and nanostructures on the copper surface.

The laser texturing using different ablation parameters clearly causes macroscopic topography effects (grooves and textures) and microscopic near-surface modifications, as well as redeposited layers. Such complex multiscale surface modifications induce changes of the material properties, as for instance the optical properties (see Fig. 6 (left)). For high laser power and low scanning speed (red zone), the reflectivity in the visible wavelength range is significantly lower than the reflectivity of the pristine surface. The low optical reflectivity (see Fig. 6 (left)) correlates with the formation of surface nanostructures (see Fig. 4).

The SEM images shown in Fig. 6 (right) are obtained using the same SEM conditions, i.e. the emissivity of secondary electrons for the primary excitation energy E_p of 5 keV is represented by the grey level of the image. The figure indicates that the high- E_p (5 keV) SEY is dependent on the laser-treatment parameters. The copper surface irradiated at high laser power and low scanning speed (red zone) has a lower SEY at 5 keV than the untreated surface. In contrast, at low laser power and high scanning speed, the SEY of the laser-treated surface exhibits a higher value than the untreated surface at $E_p=5$ keV. In addition, the SEY was determined in dependence on the primary electron energy E_p in the range between 50 and 1800 eV for selected large-area (18×18 mm²) samples as shown in Fig. 7(a). The colours of the SEY graphs correspond to the identified four different types of surface topographies. The shape of the SEY curves of the laser-treated samples is very different from the air exposed untreated Cu surface [24], which exhibits a SEY maximum δ_{max} of ~ 2.18 . $E_p=280$ eV. The most significant difference after laser-treatment is the much higher primary electron energy of the SEY maximum δ_{max} ; in most cases δ_{max} was found at the highest accessible energy of 1800 eV in the experiment. Figure 7(a) indicates that the SEY maximum is reduced for increasing laser intensities. On the other hand, for low laser intensities (e.g. high scan speeds) the SEY at 1800 eV can exceed that of pristine air exposed Cu, a fact which is in agreement with the observation in secondary electron emission at 5 keV as shown in Fig. 6 (right). In particular, the compact flower head-like nanostructures formed at high laser fluence (Fig. 5(a) (red)) exhibit a SEY maximum well below 1 in the full accessible E_p range. At $P\sim 1$ W and $v=1$ mm/s, a SEY maximum of 0.8 was obtained. The SEY maximum can be reduced to $\delta_{\text{max}}=0.7$ at $P\sim 2.46$ W and $v=2$ mm/s for the implemented UV laser. It has to be mentioned that the utilisation of UV and IR ns laser radiation allows the fabrication of similar compact nanostructures with a δ_{max} below unity [14, 36].

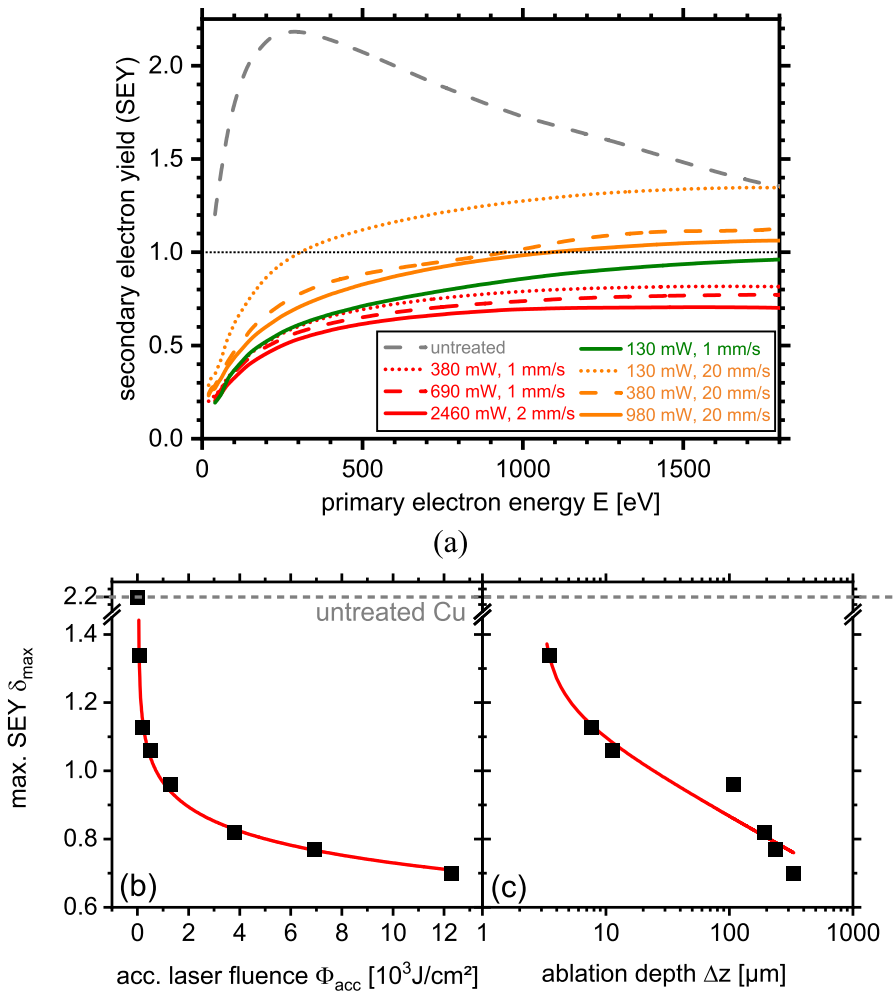


Fig. 7 **a** Energy dependence of the secondary electron yield (SEY) for laser-treated copper surfaces ($\lambda = 355 \text{ nm}$, $f = 100 \text{ kHz}$, $\Delta y = 10 \mu\text{m}$) at different scanning speed v and laser power P . **b** and **c** Secondary electron yield maximum δ_{\max} dependent on the accumulated laser fluence and the estimated ablation depth Δz (based on Eq. 7), respectively. The red lines are the results of data fitting using Eqs. 8 and 9, respectively

The non-compact nanostructures (Fig. 5 (b) (green)) exhibit a SEY maximum around unity ($\delta_{\max} = 0.96$ at $P \sim 0.13 \text{ W}$ and $v = 1 \text{ mm/s}$). The re-solidified droplet structures (6(c) (yellow)) exhibit a δ_{\max} above 1 ($\delta_{\max} = 1.06$ (1.35) for $P \sim 1$ (0.13) W and $v = 20 \text{ mm/s}$).

Similar to the optical appearance, the secondary electron yield maximum δ_{\max} is also directly dependent on the accumulated laser fluence Φ_{acc} ($\Phi_{\text{acc}} = P \cdot N / (f \cdot \pi \cdot \omega^2)$): as shown in Fig. 7(b) it decreased for increasing Φ_{acc} . The dependence can be described by means of the following empirical equation:

$$\delta_{\max}(\Phi_{acc}) = a_{\Phi} - b_{\Phi} \cdot \ln\left(\frac{\Phi_{acc} - c_{\Phi}}{1 \text{ J/cm}^2}\right) \quad (8)$$

which resulted in $a_{\Phi} = 1.66$, $b_{\Phi} = 0.101$, $c_{\Phi} = 40.62 \text{ J/cm}^2$. The experimental results suggest that there is a correlation between δ_{\max} and the ablation volume and the ablation depth, respectively. In Fig. 7(b), the SEY dependence on the ablation depth Δz (calculated by Eq. 7 under assumption of the number of laser pulses N_a for overlapping lines Eq. 2) is shown. In agreement with the accumulated laser fluence dependency, the secondary electron yield maximum decreased at increasing ablation depth and the behaviour can be described by:

$$\delta_{\max}(\Delta z) = a_z - b_z \cdot \ln\left(\frac{\Delta z - c_z}{1 \text{ }\mu\text{m}}\right), \quad (9)$$

where the experimental data and the corresponding fit are plotted in Fig. 78 (b) with the obtained fit parameters $a_z = 1.27$, $b_z = 0.09$, $c_z = 2.01 \text{ }\mu\text{m}$. It can be assumed that the determined ablation depth Δz is a measure for the experimentally determined modification depth m . Thus, the results suggest that the increase of the modification depth leads to a reduction of the maximum secondary electron yield. In this experimental setup, a lowest limit for the maximum secondary electron yield of about 0.7 was determined.

Similar effects were found for the SEY of laser-induced microscopic trenches. Bajek et al. [2] reported the SEY maximum δ_{\max} of nanostructure-covered trenches and cleaned trenches. The δ_{\max} of nanostructure-covered trenches was smaller than that of the cleaned trenches. The results suggest that the nanostructures are more important for SEY reduction than the microscopic trenches. The ablation process creates a nanostructured surface with deep trenches within the bulk material. Consequently, the laser parameters and especially the accumulated laser fluence have impact on the resulting sample topography and surface roughness as also reported by Gaidys et al. [13]. Both features, the micro-trenches and nanostructures, enhance inelastic scattering of the incoming electrons and in that sense enable an efficient way of energy dissipation that reduces the probability of secondary electron emission.

The experimental finding that δ_{\max} decreases with increasing accumulated laser fluence was also observed when irradiating copper surfaces with other laser sources. Valizadeh et al. reported that the reduction of the scanning speed or line spacing, corresponding to an increase of the accumulated laser fluence, leads to a reduction of δ_{\max} [37, 38].

Conclusions

Polycrystalline copper surfaces were textured by ps-laser irradiation at $\lambda = 355 \text{ nm}$, $f = 100 \text{ kHz}$, and $\Delta t_p = 12 \text{ ps}$. The copper ablation process was studied in dependence of the laser power and scanning velocity and an ablation threshold of 0.13 W and 0.4 J/cm^2 was determined, respectively. An incubation coefficient of 0.17 was

estimated. Test structures consisting of line arrays with a distance of 10 μm were examined to evaluate correlations between surface morphology and the secondary electron yield (SEY). The achieved surface morphologies were classified into four different categories, which form dependent on the laser processing parameters: (1) compact flower head-like nanostructures, (2) non-compact nanostructures, (3) melting structures and (4) minor surface modification. The nanostructure formation is the result of combined processes including laser ablation from the copper surface (microstructure formation), redeposition of ablated products (porous nanostructure formation) and modification/tempering of the redeposited material (modification of the redeposited nanostructures) due to locally enhanced pressure conditions (ablation pressure). The experimental results suggest that the combination of a high ablation volume (high available particle density for the redeposition process), the tempering process and a locally elevated pressure enable the formation of the compact flower head-like nanostructures (at high laser power and low scanning speed) resulting in surfaces with very low SEY maximum as low as $\delta = 0.7$.

In general, the laser-ablation induced morphological and topographical changes have significant impact on the SEY in dependence of the primary electron energy as well as on the SEY maximum. The ablation process creates a nanostructured surface with deep trenches within the bulk material. Both features enhance inelastic scattering of the incoming electrons and in that sense enable an efficient way of energy dissipation that reduces the probability of secondary electron generation and emission. The reduction of the SEY to below unity is required to efficiently mitigate electron cloud formation in particle accelerators.

Funding Open Access funding enabled and organized by Projekt DEAL.

Open Access This article is licensed under a Creative Commons Attribution 4.0 International License, which permits use, sharing, adaptation, distribution and reproduction in any medium or format, as long as you give appropriate credit to the original author(s) and the source, provide a link to the Creative Commons licence, and indicate if changes were made. The images or other third party material in this article are included in the article's Creative Commons licence, unless indicated otherwise in a credit line to the material. If material is not included in the article's Creative Commons licence and your intended use is not permitted by statutory regulation or exceeds the permitted use, you will need to obtain permission directly from the copyright holder. To view a copy of this licence, visit <http://creativecommons.org/licenses/by/4.0/>.

References

1. Abdelmalek, A., et al.: Ablation of copper metal films by femtosecond laser multipulse irradiation. *Appl. Sci.* **8**(10), 1826 (2018)
2. Bajek, D., et al.: Role of surface microgeometries on electron escape probability and secondary electron yield of metal surfaces. *Sci. Rep.* **10**(1), 250 (2020)
3. Bogaerts, A., Chen, Z., Bleiner, D.: Laser ablation of copper in different background gases: comparative study by numerical modeling and experiments. *J. Anal. Atom. Spectrom.* **21**(4), 384–395 (2006)

4. Bornschlegel, B., Finger, J.: In-situ analysis of ultrashort pulsed laser ablation with pulse bursts. *J. Laser Micro/Nanoengineering*. **14**(1), 7 (2019)
5. Büttner, H., et al.: High aspect ratio microstructuring of copper surfaces by means of ultrashort pulse laser ablation. *Procedia CIRP*. **68**, 190–195 (2018)
6. Byskov-Nielsen, J., et al.: Ultra-short pulse laser ablation of copper, silver and tungsten: experimental data and two-temperature model simulations. *Appl. Phys. A*. **103**(2), 447–453 (2011)
7. Calatroni, S., et al.: First accelerator test of vacuum components with laser-engineered surfaces for electron-cloud mitigation. *Phys. Rev. Accelerators Beams*. **20**(11), 113201 (2017)
8. Calatroni, S., et al.: Cryogenic surface resistance of copper: investigation of the impact of surface treatments for secondary electron yield reduction. *Phys. Rev. Accelerators Beams*. **22**(6), 063101 (2019)
9. Campbell, B., et al.: Shallow hole drilling with ultrashort pulse lasers. *Lasers and Applications in Science and Engineering*, vol. 6879. SPIE (2008)
10. Di Niso, F., et al.: Influence of the repetition rate and pulse duration on the incubation effect in multiple-shots ultrafast laser ablation of steel. *Phys. Procedia*. **41**, 698–707 (2013)
11. Fan, P., et al.: Angle-independent colorization of copper surfaces by simultaneous generation of picosecond-laser-induced nanostructures and redeposited nanoparticles. *J. Appl. Phys.* **115**(12), 124302 (2014)
12. Fernández-Arias, M., et al.: Fabrication and deposition of copper and copper oxide nanoparticles by laser ablation in open air. *Nanomaterials (Basel)*. **10**(2) (2020)
13. Gaidys, M., et al.: Efficient picosecond laser ablation of copper cylinders. *Appl. Surf. Sci.* **483**, 962–966 (2019)
14. Hannah, A.N., et al.: Characterisation of copper and stainless steel surfaces treated with laser ablation surface engineering. *Vacuum*. **189**, 110210 (2021)
15. Hashida, M., et al.: Ablation threshold dependence on pulse duration for copper. *Appl. Surf. Sci.* **197–198**, 862–867 (2002)
16. Jee, Y., Becker, M.F., Walser, R.M.: Laser-induced damage on single-crystal metal surfaces. *J. Opt. Soc. Am. B Opt. Phys.* **5**, 648 (1988)
17. Johnson, P.B., Christy, R.W.: Optical constants of the noble metals. *Phys. Rev. B*. **6**(12), 4370–4379 (1972)
18. Jordan, R., et al.: Pulsed laser ablation of copper. *Appl. Surf. Sci.* **86**(1), 24–28 (1995)
19. Liu, J.M.: Simple technique for measurements of pulsed Gaussian-beam spot sizes. *Opt. Lett.* **7**(5), 196–198 (1982)
20. Lopez, J., et al.: Parameters of influence in surface ablation of metals with using a high power tunable ultrafast laser. *Int. Congr. Appl. Lasers Electro-Optics*. (1), 686–694 (2013, **2013**)
21. Mur, J., et al.: High precision laser direct microstructuring system based on bursts of picosecond pulses. *J. Phys. D: Appl. Phys.* **50**(32), 325104 (2017)
22. Nicolai, H., et al.: Fundamental investigations of ps-laser burst-mode on common metals for an enhanced ablation process. In: *Proc. SPIE*. (2015)
23. Pandey, P.K., Gupta, S.L., Thareja, R.K.: Study of pulse width and magnetic field effect on laser ablated copper plasma in air. *Phys. Plasmas*. **22**(7), 073301 (2015)
24. Petit, V., et al.: Role of the different chemical components in the conditioning process of air exposed copper surfaces. *Phys. Rev. Accelerators Beams*. **22**(8), 083101 (2019)
25. Raciukaitis, G., et al.: Accumulation effects in laser ablation of metals with high-repetition-rate lasers. *High-Power Laser Ablation 2008*, vol. 7005. SPIE (2008)
26. de Rossi, W., et al.: Effects of ultrashort laser ablation in copper and stainless steel. *Lasers in Manufacturing Conference*, (2015)
27. Schäfer, C., Urbassek, H.M., Zhigilei, L.V.: Metal ablation by picosecond laser pulses: a hybrid simulation. *Phys. Rev. B*. **66**(11), 115404 (2002)
28. Schille, J., et al.: Characterisation of interaction phenomena in high repetition rate femtosecond laser ablation of metals. *Int. Congr. Appl. Lasers Electro-Optics*. **2012**(1), 949–958 (2012)
29. Schille, J., et al.: High-pulse repetition frequency ultrashort pulse laser processing of copper. *J. Laser Appl.* **27**(S2), S28007 (2015)
30. Singh, S., et al.: Effect of ambient air pressure on debris redeposition during laser ablation of glass. *J. Appl. Phys.* **98**(11), 113520 (2005)
31. Smausz, T., et al.: Study on the effect of ambient gas on nanostructure formation on metal surfaces during femtosecond laser ablation for fabrication of low-reflective surfaces. *Appl. Surf. Sci.* **389**, 1113–1119 (2016)

32. Taborelli, M.: Secondary electron yield of surfaces: what we know and what we still need to know. ECLOUD'18 Proceedings, p. 97–103, (2018)
33. Tunna, L., et al.: Micromachining of copper using Nd:YAG laser radiation at 1064, 532, and 355 nm wavelengths. *Opt. Laser Technol.* **33**(3), 135–143 (2001)
34. Valizadeh, R. and O.B. Malyshev. Apparatus and methods relating to reduced photoelectron yield and/or secondary electron yield. 2015
35. Valizadeh, R., et al.: Low secondary electron yield engineered surface for electron cloud mitigation. *Appl. Phys. Lett.* **105**(23), 231605 (2014)
36. Valizadeh, R., et al.: Low secondary electron yield of laser treated surfaces of copper, aluminium, and stainless steel. Proceedings of IPAC2016, Busan, Korea, p. 1089–1092, (2016)
37. Valizadeh, R., et al.: Reduction of secondary electron yield for E-cloud mitigation by laser ablation surface engineering. *Appl. Surf. Sci.* **404**, 370–379 (2017)
38. Valizadeh, R., et al.: Multipacting suppression by laser ablation surface engineering for space application. 10th Int. Particle Accelerator Conf. (IPAC2019), p. 1365–1368 (2019)
39. Vorobyev, A.Y., Guo, C.: Direct femtosecond laser surface nano/microstructuring and its applications. *Laser Photonics Rev.* **7**(3), 385–407 (2013)
40. Watts, C., Gilmore, M., Schamiloglu, E.: Effects of laser surface modification on secondary electron emission of copper. *IEEE Trans. Plasma Sci.* **39**(3), 836–841 (2011)
41. Yang, J., et al.: Ablation of metallic targets by high-intensity ultrashort laser pulses. *Phys. Rev. B.* **76**(16), 165430 (2007)
42. Zayarny, D.A., et al.: Pulse-width-dependent surface ablation of copper and silver by ultrashort laser pulses. *Laser Phys. Lett.* **13**(7), 076101 (2016)
43. Žemaitis, A., et al.: Advanced laser scanning for highly-efficient ablation and ultrafast surface structuring: experiment and model. *Sci. Rep.* **8**(1), 17376 (2018)
44. Žemaitis, A., et al.: Highly-efficient laser ablation of copper by bursts of ultrashort tuneable (fs-ps) pulses. *Sci. Rep.* **9**(1), 12280 (2019)

Publisher's note Springer Nature remains neutral with regard to jurisdictional claims in published maps and institutional affiliations.